
This is an electronic reprint of the original article.

This reprint may differ from the original in pagination and typographic detail.

Jurček, Ondřej; Nonappa; Kalenius, Elina; Jurček, Pia; Linnanto, Juha M.; Puttreddy, Rakesh; Valkenier, Hennie; Houbenov, Nikolay; Babiak, Michal; Peterek, Miroslav; Davis, Anthony P.; Marek, Radek; Rissanen, Kari

Hexagonal Microparticles from Hierarchical Self-Organization of Chiral Trigonal Pd₃L₆ Macrotetracycles

Published in:

Cell Reports Physical Science

DOI:

[10.1016/j.xcrp.2020.100303](https://doi.org/10.1016/j.xcrp.2020.100303)

Published: 20/01/2021

Document Version

Publisher's PDF, also known as Version of record

Published under the following license:

CC BY-NC-ND

Please cite the original version:

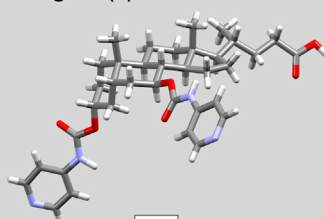
Jurček, O., Nonappa, Kalenius, E., Jurček, P., Linnanto, J. M., Puttreddy, R., Valkenier, H., Houbenov, N., Babiak, M., Peterek, M., Davis, A. P., Marek, R., & Rissanen, K. (2021). Hexagonal Microparticles from Hierarchical Self-Organization of Chiral Trigonal Pd₃L₆ Macrotetracycles. *Cell Reports Physical Science*, 2(1), Article 100303. <https://doi.org/10.1016/j.xcrp.2020.100303>

Article

Hexagonal Microparticles from Hierarchical Self-Organization of Chiral Trigonal Pd_3L_6 Macrotetracycles

A) Ursodeoxycholic Bile Acid Based Ligand (L)

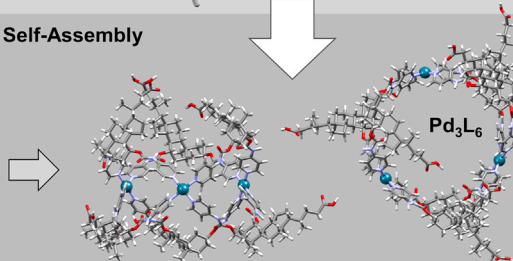
- ✓ Hetero-Tritopic
- ✓ Amphiphilic
- ✓ Amphoteric
- ✓ Chiral
- ✓ Asymmetric



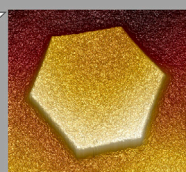
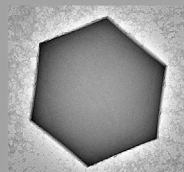
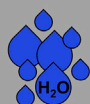
B) Transmetalation Self-Assembly

1) $\text{Cu}(\text{NO}_3)_2$

2) $\text{Pd}(\text{NO}_3)_2$



C) Self-Organization



Ondřej Jurček, Elina Kalenius, ..., Anthony P. Davis, Radek Marek, Kari Rissanen

ondrej.jurcek@ceitec.muni.cz (O.J.)
kari.t.rissanen@jyu.fi (K.R.)

HIGHLIGHTS

Asymmetric, amphiphilic, chiral, and hetero-tritopic ligand from bile acid

Supramolecular transmetalation self-assembly leads to symmetric superchiral complex

Complexes self-organize in aqueous environment into hexagonal microparticles

Materials with high density of chiral centers and optical activity are prepared

Jurček et al. report an amphiphilic bile-acid-based ligand (L) used for the preparation of large hollow metallocupramolecular complex Pd_3L_6 , accomplished via a supramolecular transmetalation process. The complexes prepared can self-organize into hexagonal microparticles upon contact with water.

Jurček et al., Cell Reports Physical Science 2, 100303

January 20, 2021 © 2020 The Author(s).

<https://doi.org/10.1016/j.xcrp.2020.100303>



Article

Hexagonal Microparticles from Hierarchical Self-Organization of Chiral Trigonal Pd₃L₆ Macrotetracycles

Ondřej Jurček,^{1,2,3,4,9,14,*} Nonappa,^{5,6,10} Elina Kalenius,³ Pia Jurček,¹ Juha M. Linnanto,⁷ Rakesh Puttreddy,³ Hennie Valkenier,^{4,8,11} Nikolay Houbenov,⁶ Michal Babiak,¹ Miroslav Peterek,¹ Anthony P. Davis,^{4,12} Radek Marek,^{1,2,13} and Kari Rissanen^{3,*}

SUMMARY

Construction of structurally complex architectures using inherently chiral, asymmetric, or multi-heterotopic ligands is a major challenge in metallosupramolecular chemistry. Moreover, the hierarchical self-organization of such complexes is unique. Here, we introduce a water-soluble, facially amphiphilic, amphoteric, chiral, asymmetric, and hetero-tritopic ligand derived from natural bile acid, ursodeoxycholic acid. We show that via the supramolecular transmetalation reaction, using nitrates of Cu(II) or Fe(III), and subsequently Pd(II), a superchiral Pd₃L₆ complex can be obtained. Even though several possible constitutional isomers of Pd₃L₆ could be formed, because of the ligand asymmetry and relative flexibility of carbamate-pyridyl moieties attached to the steroid scaffold, only a single product with C₃ rotational symmetry was obtained. Finally, we demonstrate that these amphiphilic complexes can self-organize into hexagonal microparticles in aqueous media. This finding may lead to the development of novel self-assembled metal-organic functional materials made of natural, abundant, and relatively inexpensive steroidal compounds.

INTRODUCTION

In nature, self-assembling processes of small building blocks are the basic principles for the hierarchical structural organization of biological supramolecules of all living organisms. Natural building blocks are often chiral, asymmetric, and amphiphilic molecules. During self-assembly processes, the molecules seek the lowest energy levels in agglomerates, governed by the interplay of multiple non-covalent interactions and energetic and entropic factors.¹ By mastering the self-assembly processes and understanding the structural and physicochemical properties of building blocks, scientists are now approaching the development of novel materials with unique properties via hierarchical structural design and self-organization.^{2–7} Among diverse approaches, the self-assembly of organic ligands driven by a metal coordination is a widely investigated process that allows the construction of various metallosupramolecular architectures.^{8–14} Palladium(II) is often used as an interconnecting metal center to couple ligand units.^{15–17} It has also been shown that the metal complexes can further self-organize into higher-ordered superstructures.^{3,12,13,18,19} Despite the tremendous effort in ligand design and synthesis, supramolecular chemists instead use simpler ligands whose coordination behavior can easily be predicted and controlled. The ligands used are mostly symmetric, homotopic (having one type of

¹CEITEC—Central European Institute of Technology, Masaryk University, Kamenice 5, 62500 Brno, Czechia

²Department of Chemistry, Faculty of Science, Masaryk University, Kamenice 5, 62500 Brno, Czechia

³University of Jyväskylä, Department of Chemistry, PO Box 35, 40014 Jyväskylä, Finland

⁴School of Chemistry, University of Bristol, Cantock's Close, Bristol BS8 1TS, UK

⁵Faculty of Engineering and Natural Sciences, Tampere University, PO Box 541, 33101 Tampere, Finland

⁶Department of Applied Physics, Aalto University, PO Box 15100, 00076 Aalto, Finland

⁷University of Tartu, Institute of Physics, W. Ostwald Street 1, 50411 Tartu, Estonia

⁸Université Libre de Bruxelles (ULB), Ecole Polytechnique de Bruxelles, Engineering of Molecular NanoSystems, Avenue F.D. Roosevelt 50, CP165/64 1050 Brussels, Belgium

⁹Twitter: @OndrejJurcek

¹⁰Twitter: @nonappa

¹¹Twitter: @HennieValkenier

¹²Twitter: @APDChem

¹³Twitter: @LabMarek

¹⁴Lead Contact

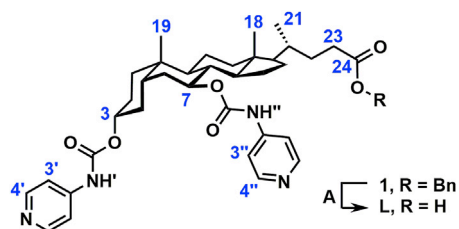
*Correspondence: ondrej.jurcek@ceitec.muni.cz (O.J.), kari.rissanen@jyu.fi (K.R.)
<https://doi.org/10.1016/j.xcrp.2020.100303>



coordination site), and achiral. The use of asymmetric (without the axis of symmetry between the binding sites, except for C_1), heterotopic, and chiral ligands in conventional metallosupramolecular chemistry is rather scarce.^{11,14,20} This is mainly attributed to (1) coordinationally overlapping binding sites in heterotopic ligands, which results in a mixture of coordination complexes instead of a single product, (2) the assumption that the metal complexation of asymmetric ligands leads to multiple isomers of metal complexes, and (3) the synthetic severity of chiral compounds. To address the above challenges, we envisaged that bile acid (BA) molecules are well-suited candidates for the preparation of heterotopic, chiral, and asymmetric ligands, and for studies of their coordination behavior with significant potential for future biological applications.²¹

As noted above, the metal coordination to heterotopic ligands may represent a significant challenge when targeting a single final product. This can be overcome by implementing a supramolecular transmetalation approach.²² In supramolecular transmetalation, the metal exchange takes place between a metal complex and either a metal salt or a different metal complex, resulting in a targeted coordination product. However, this not yet fully understood method has been used on only a few occasions when assemblies could not be accessed via direct metal-to-ligand coordination. In general, two types of supramolecular transmetalation processes can be distinguished: (1) where the direct substitution replaces one type of metal for another without changing the overall supramolecular assembly and (2) a less predictable disruptive exchange process in which the metal exchange leads to a change in the composition of the assembly.²²

BAs are composed of a hydrophobic rigid steroid backbone to which hydrophilic hydroxyl and aliphatic carboxyl groups are attached, conferring facial amphiphilicity. BAs naturally contain multiple chiral centers—for example, 10 in the case of ursodeoxycholic acid (UDCA). BAs, their salts, or conjugates can form micelles in aqueous solution, or, together with dietary cholesterol, phospholipids, and fatty acids coming from the enzymatic breakdown of triglycerides, they can form cylindrical or worm-like mixed micelles. These natural assemblies play a major role in lipid digestion and the enterohepatic circulation of mammals.^{23,24} The amphiphilic character and molecular rigidity of BAs and their derivatives (with very little conformational freedom of the side alkyl chain) are responsible for their strong aggregation behavior, which also plays an important role in their use in the field of supramolecular chemistry.^{25–28} Examples of their applications range from molecular gels^{29–32} and ion receptors^{26,28,33} to self-assembled materials and microparticles.^{7,34–37} However, their use in the metallosupramolecular chemistry of discrete species has not been pursued extensively. Recently, we have reported the preparation and characterization of a concave coordination complex, Pd_3L_6 , made of a simple homotopic bispyridyl BA-based ligand coordinating directly to $Pd(CH_3CN)_4(BF_4)_2$. The structural organization of the single constitutional isomer of Pd_3L_6 was determined by a combination of various analytical techniques and further supported by a complex study of its reversible structural transformation into a single symmetric isomer of $Pd_3L_3Cl_6$ using tetrabutylammonium chloride and subsequently back by $AgBF_4$.²¹ In contrast, here, we report the preparation of a heterotopic BA-based asymmetric ligand containing two pyridyl and one carboxyl coordination centers. More importantly, we present its unusual coordination self-assembly via a supramolecular transmetalation approach, using nitrates of Cu(II) or Fe(III), followed by the addition of $Pd(NO_3)_2$, into an analogous Pd_3L_6 complex. Unlike in our previous study, the ligand is water soluble and shows amphiphilic behavior, which was further expressed in the properties of the final complex. We show that the complex can



Scheme 1. Preparation of Ligand L
A: Pd/C, H₂, ethyl acetate/methanol.

undergo hierarchical self-organization into uniform hexagonal microparticles triggered by the addition of water to its dimethyl sulfoxide (DMSO) solution. This work thus represents a simple approach for the preparation of metal-organic materials derived from BAs, inspired by their natural properties and behavior.

RESULTS AND DISCUSSION

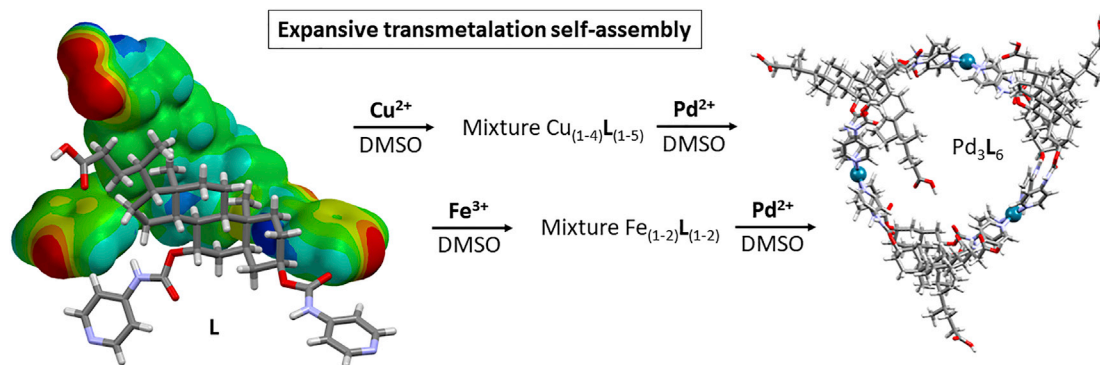
Ligand Preparation

The intermediate **1** was prepared in two steps from commercially available UDCA.²¹ Quantitative reductive cleavage of the benzyl protective group in **1** led to the hetero-tritopic ligand **L** (Scheme 1).

Ligand Self-Assembly via Supramolecular Transmetalation and Complex Characterization

In comparison to our previous work,²¹ the presence of the carboxylic acid group in addition to two pyridine binding sites within the **L** (see an illustrative electrostatic potential map of **L** in Figure S8 and Scheme 2) hampers the pyridyl-Pd²⁺ coordination and the formation of targeted Pd₃L₆ in one step. In our experiment, the simple mixing of **L** and Pd(NO₃)₂ in a 2:1 ratio in DMSO-*d*₆ led to the swift formation of insoluble precipitate with an unresolved ¹H NMR spectrum. At this point, suspecting a strong preference of Pd²⁺ for the carboxylic acid group, the one-pot synthesis of Pd₃L₆ was divided into two steps. Initially, the primary metal salt, M₁, was mixed in slight molar excess (1.1 equiv.) with **L** (3.9 mg; 6.2 × 10⁻⁵ mol) in DMSO-*d*₆ (10 mM solution), and the mixture was heated for 1 h at 55°C and analyzed using ¹H NMR spectroscopy. The use of M₁ with a strong coordination affinity with the carboxyl group and weaker coordination to pyridyls was expected to saturate the carboxyl before the second step. In the second step, the secondary salt, Pd(NO₃)₂·2H₂O (3.1 × 10⁻⁵ mol), was added and the final mixture was heated for another 1 h at 55°C, after which the ¹H NMR spectrum of the final product was recorded. Whereas coordination of primary salts such as Na⁺, K⁺, or Zn²⁺ nitrates with **L** and the subsequent addition of the secondary metal salt did not lead to the desired Pd₃L₆ complex (a similar insoluble precipitate was formed as during the direct approach), the reactions with Cu(NO₃)₂ or Fe(NO₃)₃ have successfully led to the Pd₃L₆ as followed using ¹H NMR spectroscopy (Figure 1). Moreover, we have also carried out an experiment where all of the reagents, **L**, Cu(NO₃)₂ and Pd(NO₃)₂, were mixed, dissolved in DMSO-*d*₆, and heated at 55°C in 1 step, but the experiment led to a product with an imperfect ¹H NMR spectrum (Figure S13), unlike in the 2-step approach.

The complexation of **L** with Cu²⁺ cannot be efficiently followed by ¹H NMR in solution because of the fast paramagnetic nuclear spin relaxation (open-shell system having an unpaired electron). Nevertheless, the effective binding of Cu²⁺ to pyridyl nitrogen can be monitored as a significant broadening (or even disappearance) and chemical shift of the ¹H NMR resonances of pyridyl protons and broadening and a decrease in the intensity of the adjacent carbamate –NH– signals together with their



Scheme 2. Expansive Supramolecular Cu^{2+} - or Fe^{3+} -Transmetalation Self-Assembly Leading to Pd_3L_6 Complex

slight deshielding (Figures 1A and 1D). The paramagnetic NMR signal originating from the pyridyl protons was eventually found at ~ 26 ppm at 293.2 K using a variable temperature ^1H NMR experiment (Figure S14). Shielding of H-3 and H-7 (atom numbering in Scheme 1) and the overall broadening of ^1H resonance lines of the steroid skeleton are another significant change in the ^1H NMR spectrum. Subsequently, the addition of $\text{Pd}(\text{NO}_3)_2$ in the second step induces transmetalation, and Pd^{2+} replaces Cu^{2+} at the pyridyl binding sites, as can be observed by the re-appearance of pyridyl ^1H NMR signals in the aromatic region (Figure 1E). The pyridine- Pd^{2+} coordination leads to a significant ^1H NMR deshielding of the carbamate $-\text{NH}-$ and pyridyl H-3' and H-3'' atoms, and to a slight NMR shielding effect at pyridyl H-4' and H-4'' as compared to free L. Importantly, the number of ^1H NMR signals for the final complex corresponds to that for L, indicating that the self-assembled product is highly symmetric.

Interesting observations can also be made following the ^1H NMR signal of carboxylic acid hydrogen. For example, in the case of free ligand (not coordinated with metal ions), the ^1H resonance signal corresponding to carboxylic acid hydrogen is broad and of low intensity because of its faster exchange dynamics compared to the NMR timescale. This could be caused by a strong hydrogen bonding (HB), for example, among ligand molecules, between the carboxylic acid and pyridyl groups, which was found to play an important role in the crystal packing of L, as shown later. However, this hypothesis has been dismissed following the results of the ^1H NMR dilution experiment or by the comparison of the spectra of L with its sodium salt (for details, see Figures S5 and S6, respectively). It is more probable that the ligand forms HB with solvent molecules, $\text{DMSO}-d_6$, and/or water. The strong HB can cause a greater chemical shift of the $-\text{COOH}$ proton of L (Figure 1A). In the first reaction step, upon the addition of Cu^{2+} , we can observe the narrowing and sharpening of the carboxylic acid hydrogen NMR signal. This may be caused by a weak interaction of carboxyl with free Cu^{2+} (added in excess), which slows down the exchange dynamic effect. To the contrary, strong Cu^{2+} coordination to carboxyl would lead to a disappearance of the NMR signal, which is not the case. The same effect can also be seen after the addition of Pd^{2+} (the concentration of free Cu^{2+} salt further increases to ~ 12 mM after being released by Pd^{2+} from the pyridyl binding sites). The significant chemical shift of $-\text{NH}-$ groups as well as the unprecedented larger broadening of the β -pyridyl protons when compared to α -protons can be explained by a possible slowing down of pyridyl rotational dynamics upon metal coordination and the possible through space $\beta\text{-H}\cdots\text{O}=\text{C}$ interaction (Figure S19), which

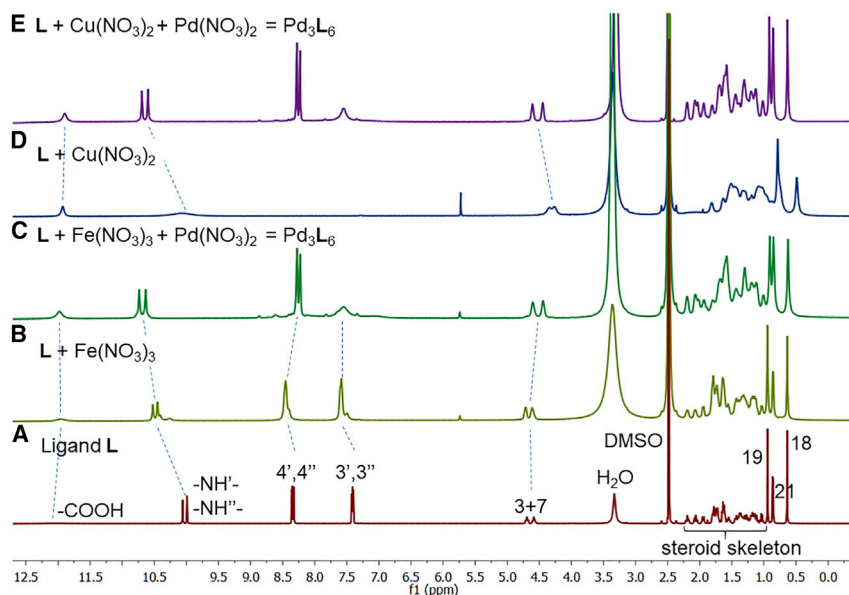


Figure 1. Comparison of ^1H NMR Spectra (in $\text{DMSO}-d_6$ at 293.2 K at 700 MHz)

(A) Ligand (L).

(B) Mixture of Fe^{3+} -ligand complexes.

(C) Final $\text{Pd}_3(\text{L})_6$ complex (Fe-transmetalation).

(D) Mixture of Cu^{2+} -ligand complexes.

(E) Final $\text{Pd}_3(\text{L})_6$ complex (Cu-transmetalation).

Increasing water content corresponds to additions of metal salt hydrates, $\text{Fe}(\text{NO}_3)_3 \cdot 9\text{H}_2\text{O}$, $\text{Cu}(\text{NO}_3)_2 \cdot 3\text{H}_2\text{O}$, and $\text{Pd}(\text{NO}_3)_2 \cdot 2\text{H}_2\text{O}$.

See also [Figures S1–S4](#) and [S9–S14](#).

may also lead to an induced electron transfer from the $-\text{NH}-$ group, causing the extra deshielding. In addition, anisotropic effects, solvent effects, and possible solvent coordination can play an important role in the overall signal shape and distribution in the NMR spectra.

The addition of $\text{Fe}(\text{NO}_3)_3$ as a primary metal salt leads to a deshielding of $\text{H}-4'$, $\text{H}-4''$ and $\text{H}-3'$, $\text{H}-3''$ pyridyl protons and of carbamate $-\text{NH}-$ signals ([Figure 1B](#)). The major set of pyridyl signals is accompanied by a similar smaller set corresponding to a second coordination species. Therefore, we can assume that at least two species are present in the solution. The interaction of L with Fe^{3+} similarly leads to a sharpening and an increase in the signal intensity of the carboxylic acid proton. In the second step, the reaction with $\text{Pd}(\text{NO}_3)_2$ also leads to a significant deshielding of the carbamate $-\text{NH}-$ signal and the pyridyl $\text{H}-3'$ and $\text{H}-3''$ signals, and to a slight shielding of pyridyl $\text{H}-4'$ and $\text{H}-4''$ as compared to the spectrum of L. These changes are attributed to the successful Pd^{2+} -pyridyl complexation ([Figure 1C](#)) and formation of the Pd_3L_6 . The NMR spectra of the final product obtained by Cu^{2+} - and Fe^{3+} -transmetalation approach are identical.

The fine coordination equilibria between Cu^{2+} and Pd^{2+} or Fe^{3+} and Pd^{2+} , pyridyls, and the carboxylic acid group are efficiently stirred toward the targeted stable Pd_3L_6 product. The two-step mechanism of supramolecular transmetalation based on the ^1H NMR spectroscopy is similar in both cases: (1) the M_1 binds to pyridyls, forming a coordination complex or complexes, and (2) the addition of Pd^{2+} leads to the replacement of M_1 from the pyridyl coordinating sites, leading to Pd_3L_6 .

The interaction of Cu^{2+} with ligand was followed by electrospray ionization-mass spectrometry (ESI-MS) (Figure S17A), showing a mixture of smaller complexation products or fragments $\text{Cu}_{(1-3)}\text{L}_{(2-4)}^+$: $[\text{L}+\text{H}]^+$, $[\text{Cu}(\text{II})\text{L}_2]^{2+}$, $[\text{Cu}(\text{II})_2\text{L}_2-2\text{H}]^{2+}$, $[\text{Cu}(\text{II})\text{L}_2-\text{NO}_3]^{2+}$, $[\text{Cu}(\text{II})_2\text{L}_3-2\text{H}]^{2+}$, and $[\text{Cu}(\text{II})_2\text{L}_4-2\text{H}]^{2+}$ (Table S1). Large Cu complexes $[\text{Cu}(\text{II})_2\text{L}_2-2\text{H}]^{2+}$, $[\text{Cu}(\text{II})_2\text{L}_3-2\text{H}]^{2+}$, and $[\text{Cu}(\text{II})_3\text{L}_4-3\text{H}]^{2+}$ have also been studied by ion-mobility mass spectrometry (IM)-MS analysis (Figure S17A) giving broad signals at 25.71, 31.33, and 36.18 ms, respectively, indicating a presence of several similar conformational isomers with a certain degree of flexibility. The use of Fe^{3+} also led to various complexes—for example, $[\text{L}+\text{H}]^+$, $[\text{Fe}(\text{III})\text{L}+\text{DMSO}]^+$, or $[\text{Fe}(\text{III})_2\text{L}_2+\text{H}]^{2+}$ —but it was challenging to assign the larger species with certainty (Figure S17B; Table S2). In both cases, the deprotonation of L is significant, decreasing the charge states of positive ions and ultimately increasing their gas phase stability. The difference in composition of Cu^{2+} - and Fe^{3+} -metallocomplexes to the Pd_3L_6 is given by the difference in coordination geometry, charge, and Lewis acid character, and thus the stability of the coordination bond. All of the M_1 complexes detected are smaller than $(\text{M}_1)_3\text{L}_6$, in which the largest ion detected is $[\text{Cu}(\text{II})_4\text{L}_5-5\text{H}]^{3+}$ (Table S1). Therefore, the formation of the large Pd_3L_6 complex from these smaller complexes can be described as expansive supramolecular transmetalation self-assembly (Scheme 2).

The formation of the Pd_3L_6 complex was confirmed by ESI-MS, showing an intense peak at m/z 686.0 corresponding to the $[\text{Pd}_3\text{L}_6]^{6+}$ ion (Figure 2; Table S3). The distribution of fragments in both spectra is identical, suggesting that the choice of M_1 does not affect the final structure of Pd_3L_6 . No adducts of Pd_3L_6 either with Cu^{2+} or with Fe^{3+} were found in the mass spectra, suggesting that these metal cations do not form stable complexes with the Pd_3L_6 .

Considering the structural asymmetry of the ligand, the symmetry of the complex identified by the ^1H NMR spectrum, and results obtained from the MS measurement, 2 constitutional isomers of Pd_3L_6 with the C_3 rotational symmetry could have been formed (Figure 3). In both isomers, 6 ligands are interconnected by 3 square-planar Pd^{2+} centers (PdN_4 coordination sphere) organized into 2 cycles containing 3 ligands each in repeating directionality C-3-pyridyl \rightarrow C-7-pyridyl, but differing in the orientation to each other. In the first isomer, the 2 cycles travel in the same direction, forming a flower-like complex, C_F (Figures 3A, 3B, and S18A; Video S1). In the second possible organization, the 2 cycles are oriented in opposite directions creating a barrel-like complex, C_B (Figures 3C, 3D, and S18B; Video S2).

The Pd_3L_6 complex obtained from the Cu^{2+} -transmetalation approach was also characterized by ESI-IM-MS.³⁸ The ESI-IM-MS analysis with N_2 drift gas for $[\text{Pd}_3\text{L}_6]^{6+}$ ion gives a sharp peak in arrival time distribution (ATD) at 20.43 ms (Figure 2A; Supplemental Experimental Procedures), indicating that a single stable conformer is present in the gas phase. The experimental collision cross-section $^{\text{DT}}\text{CCS}_{\text{He}}$ of $[\text{Pd}_3\text{L}_6]^{6+}$ measured using He as drift gas is 919.4 \AA^2 , which corresponds roughly to a diameter of 3.4 nm (assuming a spherical structure of the ion). Theoretical collision cross-section values $^{\text{DTM}}\text{CCS}_{\text{He}}$ were calculated on the basis of computational models C_F (921.2 \AA^2) and C_B (873.5 \AA^2) (Figure 3) and show that the structure for isomer C_F corresponds well to the experimental CCS of 919.4 \AA^2 . The difference between theoretical and experimental values is only $\sim 0.2\%$, which can be considered an excellent fit. ESI-IM-MS ATD for the product obtained by the Fe^{3+} -transmetalation approach is almost identical (20.34 ms; Figure 2B).

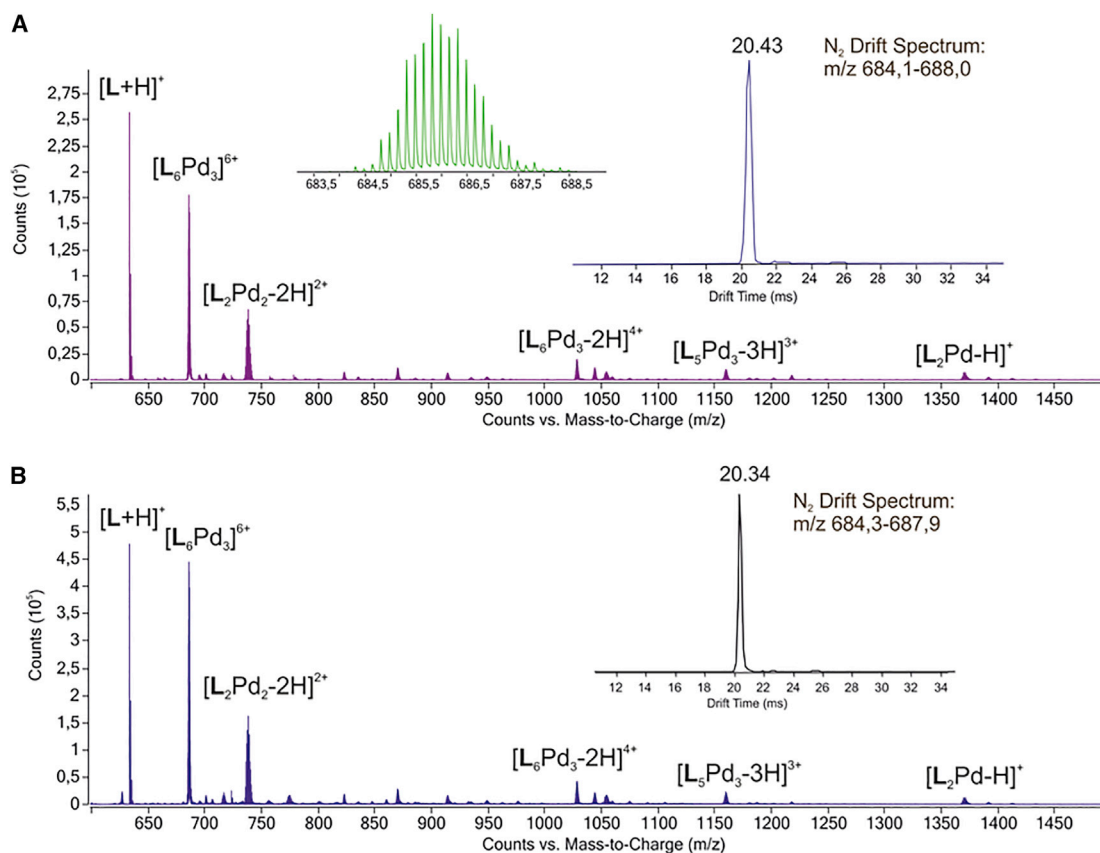


Figure 2. (+)ESI-MS Analysis of Pd₃L₆ Complex Complemented by Its IM-MS Analysis

Arrival time distribution (ATD) for peaks at m/z 686.0 shown in inset.

(A) Product obtained by supramolecular Cu²⁺-transmetalation reaction.

(B) Product obtained by supramolecular Fe³⁺-transmetalation reaction.

See also [Figure S17](#) and [Tables S1–S3](#).

To further investigate the structure of the Pd₃L₆ complex prepared via Cu²⁺-transmetalation, we have carried out ¹H DOSY (diffusion-ordered spectroscopy) NMR experiments showing the presence of a single species corresponding roughly to a hydrodynamic diameter of 3.7 nm ($D = 6.62 \times 10^{-11} \text{ m}^2 \text{ s}^{-1}$, $\log D = -10.18$, DMSO-*d*₆, 303 K) ([Figure S15](#)). This value is in good agreement with the 3.4 nm diameter in the gas phase, calculated from ^{DT}CCS_{He} of the ESI-IM-MS spectrum and with the 3.5 nm diameter measured from the computational model of C_F (while the diameter of C_B would be 3.2 nm). Furthermore, the comparison of the ground-state energies of the molecular models of C_F and C_B optimized using the density functional theory (DFT) method (for more details, see [Supplemental Experimental Procedures](#)) shows that $E_F < E_B$, where $\Delta E = E_B - E_F = 45 \text{ kcal mol}^{-1}$. Thus, C_F is clearly thermodynamically more stable, which further supports our conclusion regarding the structural organization of the Pd₃L₆ complex.

The chirality of the complex C_F, counting 60 chiral centers, was studied by circular dichroism. The experimental data were also compared with those obtained by computational calculations ([Figure 4](#)). The experimental results resemble those observed previously for flower-like complex Pd₃(1)₆,²¹ which further confirms the structural organization of C_F.

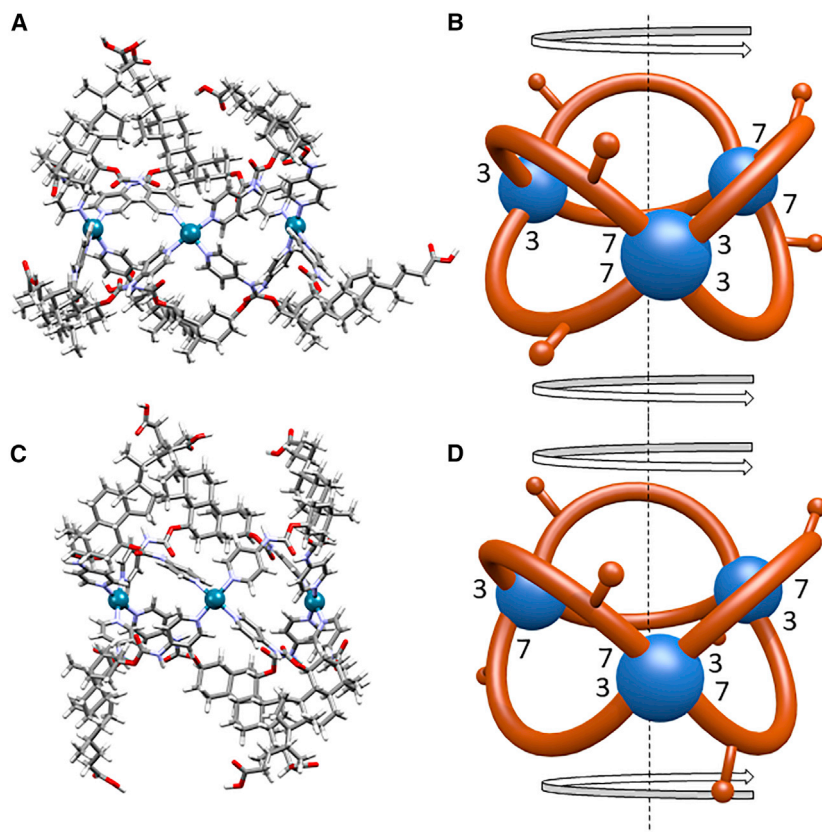


Figure 3. Computational Models of Pd₃L₆ Isomers

(A) Optimized molecular model (CAM-B3LYP) of flower-like constitutional isomer C_F.

(B) The schematic representation of the side view (A) of C_F.

(C) Optimized molecular model (CAM-B3LYP) of barrel-like constitutional isomer C_B.

(D) The schematic representation of the side view (C) of C_B.

See also [Figures S18 and S19](#).

In the previous study, the flower-like structure of Pd₃(1)₆ was confirmed by a complex structural transformation analysis.²¹ This was not possible to perform with the current system because of its complexity; however, the comparison of available structural data of Pd₃L₆ with the previously published Pd₃(1)₆ are in good agreement ([Figures S26–S28](#)), thus confirming our conclusions that the Pd₃L₆ complex resembles the flower-like structural organization.

Self-Organization Process of C_F Complexes and Particle Characterization

The carboxylic acid group in the ligand supports water solubility and amphiphilicity. It also adds to the number of available hydrogen-bond donor/acceptor groups, which could increase the chances for the preparation of X-ray-quality single crystals of C_F. Unfortunately, despite various crystallization attempts, our effort was not rewarded. However, an interesting and unprecedented observation was made. The addition of Milli-Q water to a solution of C_F in DMSO of the Cu²⁺-transmetalation reaction (~1.7 mM C_F, 10 mM L) leads to C_F aggregation. Initially, small additions of water and vigorous stirring cause foaming of the solution, a sign that C_F has the ability to act as a surface-active compound (surfactant) and that the amphiphilic character of L is translated into the character of the whole complex. In our experiments, the DMSO-d₆ solution of C_F was gradually mixed with aliquots of Milli-Q

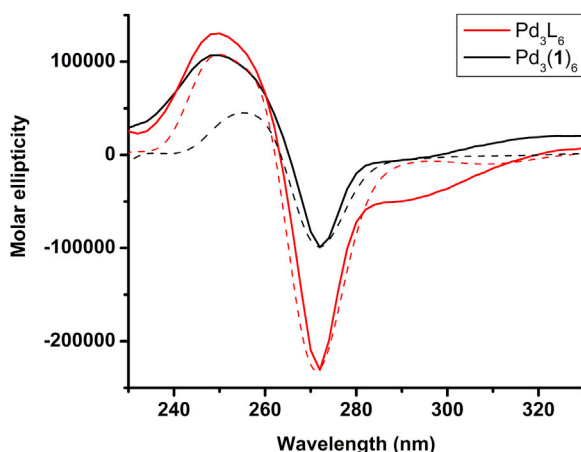


Figure 4. Electronic Circular Dichroism Spectra

Comparison of electronic CD spectra expressed in molar ellipticity of $\text{Pd}_3(\text{L})_6$ and $\text{Pd}_3(1)_6$ (methanol:DMSO mixture 500:1); experimental and simulated spectra are shown with solid and dashed lines, respectively. The simulated spectrum is normalized with the negative CD band maximum.

water. Initial water additions gradually increase the viscosity of the solution (all the way down to 50 vol% of DMSO C_F solution) to a point where the sample appears as a viscous gel-like fluid. Subsequent water additions slightly decrease the viscosity of the solution, yet the milky appearance remains (as it was continuously followed down to 10 vol% of DMSO C_F solution). A similar experiment with C_F DMSO- d_6 solution was also carried out using D_2O and followed by the ^1H NMR spectroscopy (Figure S21).

After each water addition, the sample was subjected to studies by polarized light optical microscopy (POM) in its wet form, suspecting a possible formation of lyotropic liquid crystal phase, but also in its dry state. None of the wet samples has shown birefringence, meaning that they behave as a true isotropic liquid. Evaporating the solutions to dryness yielded iridescent films on several occasions, where microparticles can be observed in their structure (Figures 5A–5C).

The films were studied in more detail by scanning electron microscopy (SEM) imaging (Figures 6A and 6B), observing uniform highly symmetric hexagonal particles throughout the samples, with side dimension 780 nm, diameter 1.6 μm , and ~ 350 nm particle thickness (Figure S22). Cryo-SEM of selected wet samples has not indicated the presence of such assemblies. Further studies on the particle morphology were subsequently done using transmission electron microscopy (TEM) (Figures 6C and 6D), electron tomographic reconstruction of TEM images (Figure 6E; Video S3), and atomic force microscopy (AFM) (Figure 6F). Cryogenic (cryo)-TEM has also been performed on wet samples, but the samples appeared amorphous. Therefore, we can conclude that the particles were being formed only during the evaporation of the solvent mixture and only at certain C_F concentrations and water:DMSO ratios (Table S4). The process of particle formation can thus be described as evaporation-induced self-assembly. Energy-dispersive X-ray (EDX) spectroscopic mapping of isolated hexagonal particles (Figure S24) confirmed that the particle composition is similar to that of C_F ; thus, the particles are built of C_F supramolecules. Besides the presence of palladium in the EDX spectrum, Cu has also been found, suggesting that it plays a role in the particle formation. We

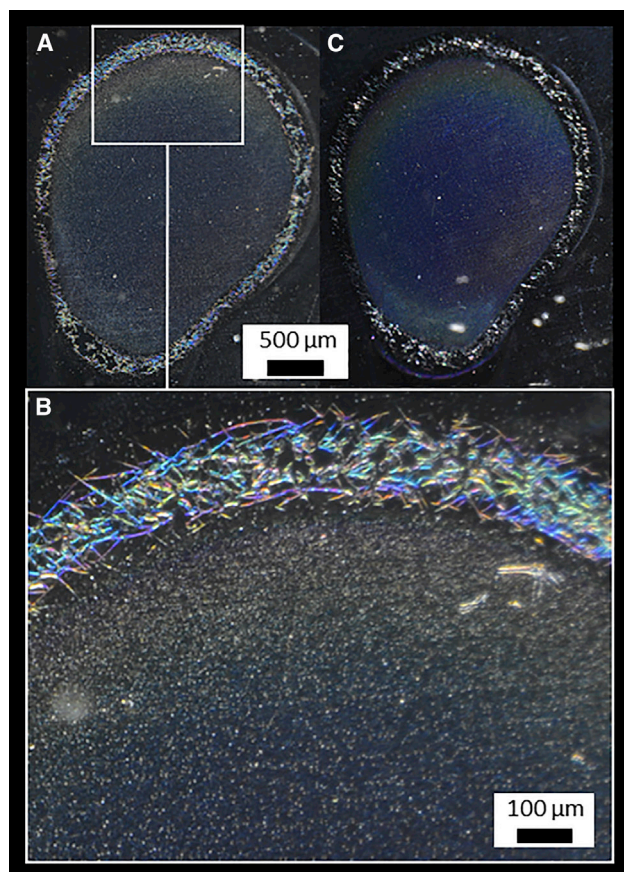


Figure 5. Polarized Light Optical Microscopy of Microparticles

(A) POM image of the sample dried containing C_F microparticles.

(B) Magnified image of the sample, in which each spot represents a single microparticle (the iridescence of the rim is caused by light refraction on the cracks of the film).

(C) The sample shows iridescence when tilted toward the light source.

have also found that the Cu^{2+} concentration has an impact on the particle formation: using either an excess, a smaller amount, or trying to remove it fully using EDTA, these experiments did not lead to particle formation upon water addition or led to a significant decrease in their yield. Even though we carried out numerous experiments to provide deeper insights into the particle structural organization, we were not able to find the exact function of Cu^{2+} . Also, not having any direct analytical proof of interaction of the Pd_3L_6 complex with Cu^{2+} , we assume that its participation in particle formation is through non-covalent interactions of its solvated structure. In contrast, the Fe^{3+} - C_F solution can similarly undergo gelation upon water addition, but the resulting mixture does not lead to the hexagonal microparticles as it was followed by SEM. The presence of Cu^{2+} is thus essential for the particle formation.

The background of the particle formation has been further investigated. It has been found that water is likely the only solvent that can induce C_F aggregation and particle formation; neat DMSO or mixtures with other polar solvents such as methanol, ethanol, or acetonitrile did not lead to any visual changes and did not induce the particle formation as verified by SEM. Studies of the water:DMSO ratio needed for particle formation suggest that 10%–50% water mixtures are optimal, but also larger

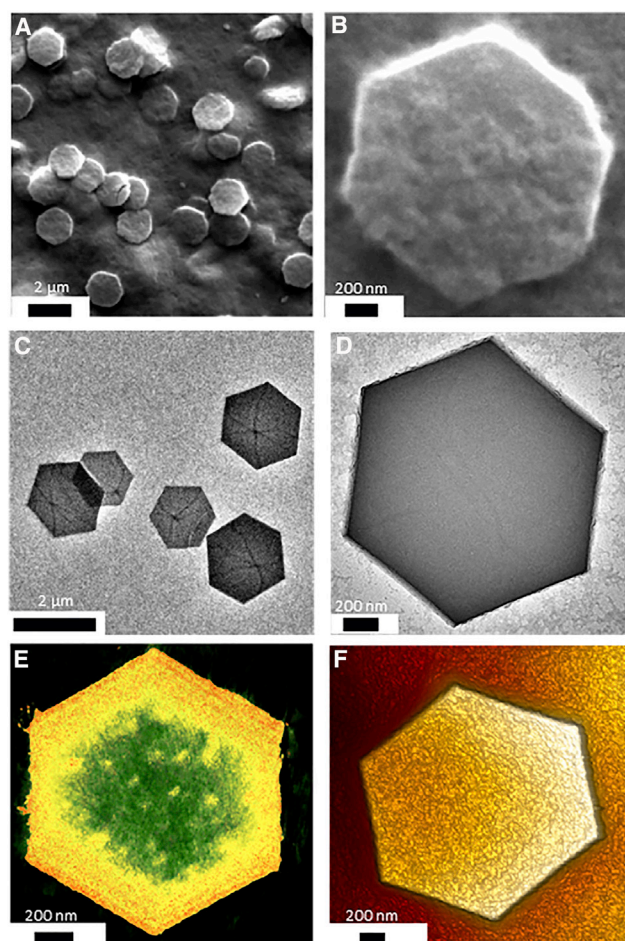


Figure 6. Electron Microscopy Images and 3-Dimensional (3D) Reconstruction of Microparticles

(A and B) Images obtained by SEM.

(C and D) Images obtained by TEM.

(E) Electron tomographic reconstruction and 3D visualization obtained using series of 2D TEM projections.

(F) Image obtained by AFM.

See also [Figure S22](#).

amounts of water added may lead to particle formation ([Table S4](#)). Nevertheless, at higher water content and higher dilution of C_F , only micelle-like tubular structures can occasionally be found in an amorphous material ([Figure S23](#); [Table S4](#)).

An attempt was made to determine the structural organization of C_F molecules in hexagonal microparticles using cryo-EM in the diffraction mode. The fresh samples prepared by the vitrification of a thin layer of the water:DMSO mixture did not contain any observable particles. Slow evaporation of the mixture close to dryness and subsequent freezing led to samples abundant with particles, but no or very low electron diffraction on the particles has been observed ([Figure S25](#)), indicating no long-range structural order. It can often be the case that long-range order is difficult to maintain in soft materials (e.g., in gels or micelles, which lack crystallinity), but also the long-range order may easily be disturbed by a certain level of structural flexibility (e.g., of side alkyl chains bearing the carboxylic acid group in our ligand).

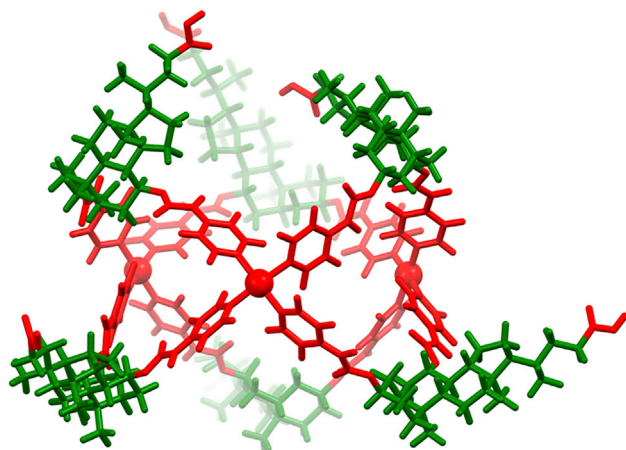
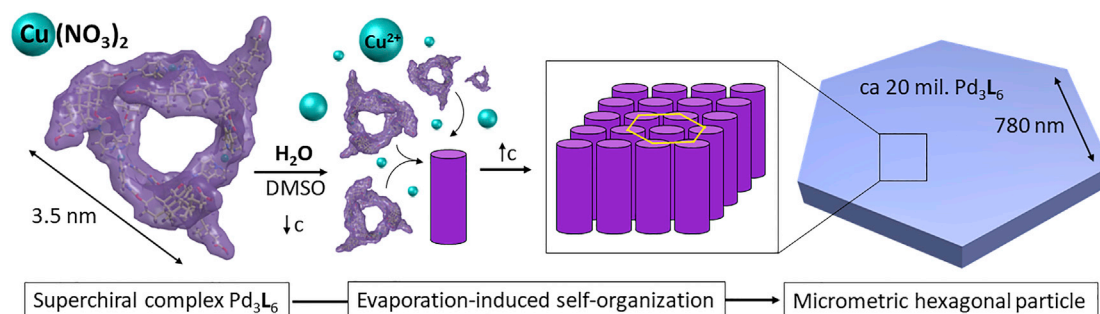


Figure 7. Polarity Zones of C_F Surfactant Molecule

Red represents polar zones and green represents non-polar zones (steroid skeletons). See also Figure S20.

In general, surfactant self-assembly is a process governed by two opposing forces: the attractive interaction between the surfactant molecules due to the hydrophobic effect, which makes the molecules associate, and the repulsive interaction due to the electrostatic or steric repulsion between the hydrophilic groups facing toward the aqueous environment. A balance needs to be achieved at certain interfacial areas between the surfactants and the aqueous environment. Based on simple theoretical models and the experimental results of known surfactants, the structural organization of assemblies can usually be estimated.³⁹ It is well documented in the literature that the “packing parameter” P can be used to establish a correlation between the surfactant molecular structure and its self-assembled morphologies. For conventional amphiphiles, the packing parameter is defined as $P = V/a_0l_c$, where V is the hydrocarbon core volume, a_0 is the equilibrium area per molecule at the interface, and l_c is the extended length of the hydrocarbon tail. Depending on the length of the hydrocarbon tail and head group, the molecules can attain the shape of a cone ($P < 1/3$), wedge ($1/3 < P < 1/2$), truncated cylinder ($1/2 < P < 1$), and cylinder ($P > 1$), leading to spherical micelles, cylindrical micelles, vesicles, and bilayers, respectively.⁴⁰ This concept is also well explored for block-co-polymer self-assembly using soluble and insoluble blocks and appropriate solvent combinations.⁴¹ However, steroidal derivatives including bile salts have been shown to deviate from the conventional surfactants’ self-assembly pathways because of their unique molecular structures.^{40,42–44} For example, BAs functionalized with allyl glycidyl ether oligomers possessing the hydrogen bonding end of the molecule have shown to form wedge-shaped amphiphiles. These amphiphiles have been further shown to form micelles in DMSO, and upon exchange to water, the micelles transformed into fibers/bilayers because of changes in packing induced by HB dimerization of the amphiphiles.³⁵ Similarly in our case, having the unconventional amphiphilic structure of C_F , the self-assembly morphologies using conventional packing parameters cannot be established with certainty. However, a theoretical deduction of the self-assembly process can be made. The facial amphiphilic nature of C_F is evident as all carboxylic acid groups face one side of the complex—the top—while the hydrophobic parts form the bottom of the complex, and the (carbamate-pyridine)₄-Pd cationic moieties are rather buried in this hydrophobic core (Figures 3A and 3B). The hollow molecule of C_F can be subdivided further into several zones based on their



Scheme 3. Hypothetical Self-Organization of Nanoscale Pd₃L₆ Complexes into Micrometric Hexagonal Particles

polarity (Figure 7; Video S4, and the complementary electrostatic potential map of L in Figure S8 and S19). Two non-ionic polar zones are represented by six carboxylic acid functionalities (3+3) organized horizontally to each other; third ionic polar zone is represented by three Pd²⁺ ions coordinated to six pyridyls with adjacent carbamate groups. Two hydrophobic non-polar regions are represented by steroid hydrocarbon skeletons (3+3). The simplified model of the C_F molecule resembles a triangular frustum (Figure S20); based on this, we can estimate the formation of cylindrical assemblies at lower concentrations as observed by SEM (Figure S23), subsequently followed by the formation of normal hexagonal assemblies at higher concentrations, in our case during the gradual solvent evaporation, when the formation of hexagonal particles happens (Scheme 3).

Moreover, the molecule of C_F is a cationic surfactant having the 6+ charge, and it is highly anisotropic and structurally rigid. The overall charge of the assembly and the surface charge density also play an important role and can present an intrinsic constraint prohibiting particle growth over a certain size. As mentioned earlier, the assemblies built of ionic surfactants are held together by short-range attractive forces that are essentially pairwise additive and by long-range electrostatic interactions. As a result, the repulsive electrostatic part of the interactions in the assembly grows faster with the size of the aggregate than the attractive part, resulting in a decrease in the potential energy, which can ultimately be the limiting factor for the growth of the assembly.⁴⁵ We assume that similar factors can also be responsible for the presence of uniform particles in our samples.

In line with our observations and the available general knowledge on the behavior of the surfactants, the formation of microscopic hexagonal particles can be attributed to the hydrophobic effect induced by water addition and partial solvation of the C_F molecule (e.g., bridging water or DMSO molecules), which is likely complemented by intermolecular HB among the polar carboxyl and/or carbamate groups of C_F, aided by the presence of inorganic salt (i.e., Cu(NO₃)₂) and further supported by the conformational rigidity of C_F. Some of these intermolecular interactions and structural features can also be seen to play a major role in the crystal packing of L (Figure S7).

In conclusion, this work describes the use of an asymmetric, hetero-tritopic, amphoteric ligand and the preparation of a large superchiral Pd₃L₆ flower-like complex via Cu²⁺- or Fe³⁺-mediated expansive supramolecular transmetalation self-assembly, which is an important approach for the synthesis of several hardly accessible metal complexes. The approach shown can, more generally, serve as a guide for controlled coordination of hetero-multitopic and even amphoteric ligands containing

pyridyl and carboxylic acid-binding sites. The successful utilization of this simple one-pot two-step synthetic approach can help to widen the library of ligands to be used in coordination supramolecular and material chemistry, in which the use of such ligands is rather scarce and possibly even deliberately avoided as being challenging. However, as shown herein, such chemical composition of ligands is desirable, bringing the key physicochemical properties to a supramolecular complex. The ligand used in this work carries structural and functional information encoded in the scaffold of the parental amphiphilic bile acid, which can be translated further into the properties of the Pd_3L_6 complex. The shape of the supramolecular complex and various types of intermolecular interactions ultimately drive its organization, triggered by the addition of water, into a higher symmetric system of hexagonal microparticles. This process resembles the aggregation of natural bile acids, which, nevertheless, usually results in smaller asymmetric assemblies of low periodicity (no more than 40 molecules of BAs), unlike in our system, in which we can estimate the participation of ~ 20 million C_F molecules in the formation of a single particle. Our work thus introduces a simple approach to the hierarchical structural design of microscopic structures derived from natural products. This artificial bile-acid-based coordination system may represent the renaissance of bile acids in supramolecular and material chemistry, having a significant potential for applications in various fields.

EXPERIMENTAL PROCEDURES

Resource Availability

Lead Contact

Further information and requests for resources and reagents should be directed to and will be fulfilled by the Lead Contact, Ondřej Jurček (ondrej.jurcek@ceitec.muni.cz).

Materials Availability

All unique reagents generated in this study are available from the Lead Contact with a completed materials transfer agreement.

Data and Code Availability

The accession number CCDC 1953708 for the supplementary crystallographic data of the ligand L reported in this paper can be obtained free of charge via https://www.ccdc.cam.ac.uk/data_request/cif, by e-mailing data_request@ccdc.cam.ac.uk, or by contacting the Cambridge Crystallographic Data Centre (12 Union Road, Cambridge CB2 1EZ, UK; fax: +44 1223 336033). Otherwise, the published article includes all of the important datasets generated or analyzed during this study. This study did not generate any code.

NMR Spectroscopy

^1H - and ^{13}C -NMR spectra were recorded on a Bruker DRX 500 MHz, a Bruker Avance 400 MHz, or Bruker Avance III HD 700 MHz or 600 MHz spectrometers. ^1H -DOSY NMR experiments were recorded on a 700-MHz Bruker Avance III NMR spectrometer. All NMR spectra are referenced to the residual internal solvent signal of $\text{DMSO}-d_6$ (2.5 ppm and 39.52 ppm for ^1H and ^{13}C , respectively).

Attenuated Total Reflection Infrared Spectroscopy

ATR-IR spectra were recorded on a Bruker Tensor 27 with mid-infrared spectroscopy (MIR) source and DLaTGS as a detector. The instrument was equipped with a Glad-iATR Diamond Crystal Plate from Pike Technologies.

IM-MS

IM-MS experiments were performed with the Agilent 6560 IM-QTOFMS instrument, which was equipped with an ESI ion source. The samples used for analyses were dissolved in DMSO- d_6 and then diluted in acetonitrile. The samples were injected by direct infusion with syringe pump using a 5- μ L/min flow rate.

The parameters were optimized to achieve maximum abundance of the ions under study. Gas temperature of 275°C, drying gas flow 5 L/min, nebulizer pressure 10 psi, and capillary voltage 5,000 V were set as source parameters. Mass spectra were externally calibrated by the ESI Tuning mix (Agilent Technologies). The charge states and composition of the ions were determined by comparison of theoretical isotopic distribution calculated based on the natural abundances of elements. The compositions of the ions were finally verified by comparing experimental m/z values with the theoretical values.

In IM-time-of-flight (TOF) experiments, the drift tube entrance and exit voltages were set as 1,674 and 224 V, respectively. As a trap filling time 20,000 μ s was used and a trap release time 150 μ s was used. Before the introduction of samples, ES tuning mix (Agilent Technologies) was measured as a reference for CCS values and to ensure stable conditions for CCS determination.^{46,47} For stepped-field measurements with He as a drift gas, the drift tube entrance voltage was varied between 563 and 876 V with 52-V increments. The data were analyzed using the MassHunter IM-MS Browser (version B08.00, Agilent Technologies).

Theoretical $^{DTM}CCS_{He}$ values were calculated with IMoS.⁴⁷ Theoretical CCS values were obtained using the trajectory method with diffuse scattering in He gas. Coordinates for calculations were obtained from DFT-calculated structures optimized at density functional CAM-B3LYP methods using the Gaussian 09 program. The number of rotations was 3, with 300,000 gas molecules per rotation. The calculations were carried out using experimental parameters (gas, temperature, and pressure).

UV-Visible (UV-Vis) and Circular Dichroism (CD) Spectroscopy

UV-vis spectra were recorded on a LAMBDA 850 spectrophotometer stabilized at 300 K. The absorbance was measured in Suprasil quartz cuvettes (10 mm, 3,500 μ L).

CD was recorded on a Jasco J-715 spectropolarimeter. CD was measured in a cylindrical Suprasil quartz cuvette (5 mm, 1,400 μ L).

Polarized Light Optical Microscopy

The Greenough stereomicroscope Leica S8 APO with apochromatic optics 1.6 \times , 8:1 zoom was used.

SEM

Scanning electron micrographs were taken with a Bruker Quantax400 EDS microscope equipped with a digital camera. Samples of the particles for SEM measurement have been prepared by transferring a small amount of sample on a sample holder (carbon-coated microscopy glass) and drying the sample under laboratory conditions in an open atmosphere. Cryo-SEM images were taken by dual-beam scanning electron microscope FEI Versa3D equipped with a gallium focused ion beam source and a Quorum cryo-stage and loading chamber.

TEM, Tomography, and Electron Diffraction

The TEM images were collected using the JEM 3200FSC field emission microscope (JEOL) operated at 300 kV in bright-field (BF) mode with an Omega-type zero-loss energy filter. The images were acquired with GATAN DIGITAL MICROGRAPH software while the specimen temperature was maintained at -187°C . The TEM samples were prepared by placing 3 μL aqueous dispersion on a 300-mesh copper grid with ultrathin carbon support film and dried under ambient conditions.

Electron tomographic tilt series were acquired with the SerialEM-software package. Samples were tilted between $\pm 69^{\circ}$ angles with 3° increment steps. Pre-alignment of the tilt image series and the fine alignment and cropping was executed with IMOD. The images were binned twice to reduce noise and computation time. A maximum entropy method (MEM) reconstruction scheme was carried out with a custom-made program on Mac or Linux cluster with a regularization parameter value of $\lambda = 1.0 \times 10^{-3}$.

Diffraction studies were performed on a FEI Talos Arctica transmission electron microscope operating at 200 kV. Micrographs were collected using a FEI CETA 16M camera.

EDX Spectroscopy

EDX spectroscopy and EDX mapping were performed using JEOL-2800 high-throughput nano-analysis field emission TEM equipped with dual large-angle dual silicon drift detectors (SDDs) EDX. The same samples as those used for TEM imaging were used under bright-field (BF) and dark-field (DF) scanning TEM (STEM) mode.

DFT Calculations

The ground-state geometries of studied structures were optimized at the DFT level by using the CAM-B3LYP functional as implemented in the Gaussian 09 program.⁴⁸ The self-consistent reaction field (SCRF) solvent model for methanol was used in the calculations. Time-dependent DFT (TD-DFT) with the CAM-B3LYP functional was used to calculate electronic transitions for the CAM-B3LYP optimized structures. Effective core potential and LANL2DZ and 6-311G(d,p) basis sets on palladium and all other atoms, respectively, were used in the calculations. It appeared that calculations overestimate transition energies, thus, the linear correlation method was used to estimate transition energies.⁴⁹ Experimental absorption band positions of the molecules and corresponding calculated transition energies gave the linear equation $E_{\text{estimated}} [\text{cm}^{-1}] = 0.688 \times E_{\text{calculated}} [\text{cm}^{-1}] + 8,839.5 \text{ cm}^{-1}$ ($R_2 = 0.998$), needed in spectral simulations. In spectral simulations, inhomogeneous broadening of the spectral lines was modeled by using Gaussian distribution of random energy disorder. One spectral simulation consisted of 10,000 iterations. The disorder (full width at half-maximum) was 2% of the value of the estimated transition energy. The Gaussian line shape function of a width of $1,800 \text{ cm}^{-1}$ was used for all of the transitions.

Single-Crystal X-Ray Crystallography

The single-crystal X-ray data for L was measured using a dual-source Rigaku Oxford Diffraction SuperNova diffractometer equipped with an Atlas detector using mirror-monochromated Cu-K α ($\lambda = 1.54184 \text{ \AA}$) radiation.⁵⁰ The data collection and reduction were performed using the program *CrysAlis^{Pro}* and a Gaussian face-indexing absorption correction method⁵⁰ was applied. The structure was

solved by using direct methods (SHELXS)⁵¹ and refined by full-matrix least-squares based on F^2 with the OLEX2 software⁵² that uses the SHELXL-2015 module.⁵¹ Some DFIX restraints were used to ensure the chemical sensibility (bond lengths and angles) of L. A few ISOR restraints and EADP constraints were used to restrict the ill-behaving thermal parameters of the structure, with a total of 52 restraints.

Crystal data for L: CCDC-1953708, $C_{162}H_{247}N_{17}O_{34}$, $M = 2,976.75$, colorless plates, $0.38 \times 0.09 \times 0.06$ mm, monoclinic, space group $P2_1$, $a = 8.8549(2)$ Å, $b = 44.2509(8)$ Å, $c = 21.3370(4)$ Å, $\beta = 95.502(2)^\circ$, $V = 8,322.1(3)$ Å³, $Z = 2$, $D_c = 1.188$ g/cm³, $F(000) = 3,220$, $\mu = 0.673$ mm⁻¹, $T = 123.0(1)$ K, $\theta_{max} = 66.750^\circ$, 83,726 total reflections, 22,479 with $lo > 2\sigma(lo)$, $R_{int} = 0.0591$, 29,255 data, 1,912 parameters, 52 restraints, $GooF = 1.048$, $R = 0.0665$ and $wR = 0.1671$ [$lo > 2\sigma(lo)$], $R = 0.0880$ and $wR = 0.1802$ (all reflections), $0.630 < d\Delta\rho < -0.704$ e/Å³, Flack = 0.08(9).

SUPPLEMENTAL INFORMATION

Supplemental Information can be found online at <https://doi.org/10.1016/j.xcrp.2020.100303>.

ACKNOWLEDGMENTS

This project has received funding from the European Union's (EU's) Horizon 2020 research and innovation programme under the Marie Skłodowska-Curie and is co-financed by the South Moravian Region under grant agreement no. 665860 (to O.J.). This publication reflects only the authors' views, and the EU is not responsible for any use that may be made of the information it contains. The Academy of Finland's Centre of Excellence in Molecular Engineering of Biosynthetic Hybrid Materials (HYBER, 2014–2019), the Photonics Research and Innovation (PREIN) flagship, and the Aalto University Nanomicroscopy Centre (Aalto-NMC) are acknowledged for access to microscopy facilities. This work was supported by the European Regional Development Fund-Project, "MSCA-fellow2@MUNI" (No. CZ.02.2.69/0.0/0.0/18_070/0009846, to P.J.). This work has received support from the Czech Science Foundation (grant no. 18-05421S to R.M.) and the Ministry of Education, Youth, and Sports of the Czech Republic (grant no. LQ1601). CIISB, Instruct-CZ Centre of Instruct-ERIC EU Consortium, funded by MEYS CR infrastructure project LM2018127, is gratefully acknowledged for the financial support of the measurements at the CFs Josef Dadok National NMR Centre and Cryo-Electron Microscopy and Tomography. H.V. is a Chercheuse Qualifiée of the Fonds de la Recherche Scientifique–FNRS. A.P.D. acknowledges the U.K. Engineering and Physical Sciences Research Council (EPSRC, grant no. EP/J00961X/1) for financial support. J.M.L. acknowledges the Estonian Research Council (grant no. PSG264) for partial support of this work. E.K. and R.P. wish to thank the Academy of Finland (projects 284562, 278743, 312514, and 298817). Dr. Anirban Som is gratefully acknowledged for the EDX spectroscopic mapping, Dr. Jan Novotný for valuable help with some NMR measurements, and M.Sc. Subhasis Chattopadhyay for recording some SEM images.

AUTHOR CONTRIBUTIONS

Conceptualization, O.J.; Methodology, O.J.; Software, J.M.L.; Validation, O.J., E.K., Nonappa, and P.J.; Investigation, O.J., Nonappa, E.K., P.J., R.P., H.V., N.H., M.B., and M.P.; Writing – Original Draft, O.J.; Writing – Review & Editing, O.J., Nonappa, E.K., P.J., R.P., H.V., J.M.L., N.H., M.B., A.P.D., R.M., and K.R.; Visualization, O.J., Nonappa, and E.K.; Supervision, O.J., A.P.D., R.M., and K.R.; Project Administration, O.J.; Funding Acquisition, O.J., A.P.D., R.M., and K.R.

DECLARATION OF INTERESTS

The authors declare no competing interests.

Received: July 27, 2020

Revised: November 12, 2020

Accepted: December 4, 2020

Published: January 8, 2021

REFERENCES

- Steed, J.W., and Atwood, J.L. (2009). *Supramolecular Chemistry* (John Wiley & Sons).
- Li, B., He, T., Fan, Y., Yuan, X., Qiu, H., and Yin, S. (2019). Recent developments in the construction of metallacycle/metallacage-cored supramolecular polymers via hierarchical self-assembly. *Chem. Commun. (Camb.)* 55, 8036–8059.
- Datta, S., Saha, M.L., and Stang, P.J. (2018). Hierarchical Assemblies of Supramolecular Coordination Complexes. *Acc. Chem. Res.* 51, 2047–2063.
- Chen, L.-J., and Yang, H.-B. (2018). Construction of Stimuli-Responsive Functional Materials via Hierarchical Self-Assembly Involving Coordination Interactions. *Acc. Chem. Res.* 51, 2699–2710.
- Lehn, J.-M. (2018). Beyond Chemical Synthesis: Self-Organization?! *Isr. J. Chem.* 58, 136–141.
- Lehn, J.-M. (2002). Toward complex matter: supramolecular chemistry and self-organization. *Proc. Natl. Acad. Sci. USA* 99, 4763–4768.
- Bertula, K., Nonappa, Myllymäki, T.T.T., Yang, H., Zhu, X.X., and Ikkala, O. (2017). Hierarchical self-assembly from nanometric micelles to colloidal spherical superstructures. *Polymer (Guildf.)* 126, 177–187.
- Wang, W., Wang, Y.-X., and Yang, H.-B. (2016). Supramolecular transformations within discrete coordination-driven supramolecular architectures. *Chem. Soc. Rev.* 45, 2656–2693.
- Zhang, J.-P., Huang, X.-C., and Chen, X.-M. (2009). Supramolecular isomerism in coordination polymers. *Chem. Soc. Rev.* 38, 2385–2396.
- Han, M., Engelhard, D.M., and Clever, G.H. (2014). Self-assembled coordination cages based on banana-shaped ligands. *Chem. Soc. Rev.* 43, 1848–1860.
- Chen, L.-J., Yang, H.-B., and Shionoya, M. (2017). Chiral metallosupramolecular architectures. *Chem. Soc. Rev.* 46, 2555–2576.
- Chen, L., Chen, Q., Wu, M., Jiang, F., and Hong, M. (2015). Controllable coordination-driven self-assembly: from discrete metallocages to infinite cage-based frameworks. *Acc. Chem. Res.* 48, 201–210.
- Smulders, M.M.J., Riddell, I.A., Browne, C., and Nitschke, J.R. (2013). Building on architectural principles for three-dimensional metallosupramolecular construction. *Chem. Soc. Rev.* 42, 1728–1754.
- Pan, M., Wu, K., Zhang, J.-H., and Su, C.-Y. (2019). Chiral metal–organic cages/containers (MOCs): from structural and stereochemical design to applications. *Coord. Chem. Rev.* 378, 333–349.
- Chakrabarty, R., Mukherjee, P.S., and Stang, P.J. (2011). Supramolecular coordination: self-assembly of finite two- and three-dimensional ensembles. *Chem. Rev.* 111, 6810–6918.
- Fujita, D., Ueda, Y., Sato, S., Yokoyama, H., Mizuno, N., Kumasaka, T., and Fujita, M. (2016). Self-Assembly of $M_{30}L_{60}$ Icosidodecahedron. *Chem* 1, 91–101.
- Kumar Chand, D., Fujita, M., Biradha, K., Sakamoto, S., and Yamaguchi, K. (2003). Metal driven self-assembly of pyridine appended ligands with cis-protected/naked Pd(II) ion: a comparative study. *Dalton Trans.* 2750–2756.
- Cook, T.R., and Stang, P.J. (2015). Recent Developments in the Preparation and Chemistry of Metallacycles and Metallacages via Coordination. *Chem. Rev.* 115, 7001–7045.
- Mamula, O., and von Zelewsky, A. (2003). Supramolecular coordination compounds with chiral pyridine and polypyridine ligands derived from terpenes. *Coord. Chem. Rev.* 242, 87–95.
- Lewis, J.E.M., and Crowley, J.D. (2020). Metallo-Supramolecular Self-Assembly with Reduced-Symmetry Ligands. *ChemPlusChem* 85, 815–827.
- Jurček, O., Bonakdarzadeh, P., Kalenius, E., Linnanto, J.M., Groessl, M., Knochenmuss, R., Ihalainen, J.A., and Rissanen, K. (2015). Superchiral Pd_3L_6 Coordination Complex and Its Reversible Structural Conversion into $Pd_3L_3Cl_6$ Metallocycles. *Angew. Chem. Int. Ed. Engl.* 54, 15462–15467.
- Carnes, M.E., Collins, M.S., and Johnson, D.W. (2014). Transmetalation of self-assembled, supramolecular complexes. *Chem. Soc. Rev.* 43, 1825–1834.
- Jenkins, G.J., and Hardie, L. (2008). *Bile Acids: Toxicology and Bioactivity* (RSC Publishing).
- Small, D.M. (1968). Size and Structure of Bile Salt Micelles. In *Molecular Association in Biological and Related Systems* *Advances in Chemistry, Volume 84*, E.D. Goddard, ed (American Chemical Society), pp. 31–52.
- Tamminen, J., and Kolehmainen, E. (2001). Bile Acids as Building Blocks of Supramolecular Hosts. *Molecules* 6, 21–46.
- Davis, A.P. (2007). Bile acid scaffolds in supramolecular chemistry: the interplay of design and synthesis. *Molecules* 12, 2106–2122.
- Nonappa, and Maitra, U. (2008). Unlocking the potential of bile acids in synthesis, supramolecular/materials chemistry and nanoscience. *Org. Biomol. Chem.* 6, 657–669.
- Valkenier, H., and Davis, A.P. (2013). Making a match for Valinomycin: steroidal scaffolds in the design of electroneutral, electrogenic anion carriers. *Acc. Chem. Res.* 46, 2898–2909.
- Svobodová, H., Noponen, V., Kolehmainen, E., and Sievänen, E. (2012). Recent advances in steroidal supra-molecular gels. *RSC Advances* 2, 4985–5007.
- Galantini, L., di Gregorio, M.C., Gubitosi, M., Travaglini, L., Tato, J.V., Jover, A., Meijide, F., Soto Tellini, V.H., and Pavel, N.V. (2015). Bile salts and derivatives: rigid unconventional amphiphiles as dispersants, carriers and superstructure building blocks. *Curr. Opin. Colloid Interface Sci.* 20, 170–182.
- Kuosmanen, R., Rissanen, K., and Sievänen, E. (2020). Steroidal supramolecular metallogels. *Chem. Soc. Rev.* 49, 1977–1998.
- Zana, R. (2005). *Dynamics of Surfactant Self-Assemblies: Micelles, Microemulsions, Vesicles and Lyotropic Phases* (CRC Press).
- Li, H., Valkenier, H., Judd, L.W., Brotherhood, P.R., Hussain, S., Cooper, J.A., Jurček, O., Sparkes, H.A., Sheppard, D.N., and Davis, A.P. (2016). Efficient, non-toxic anion transport by synthetic carriers in cells and epithelia. *Nat. Chem.* 8, 24–32.
- Qiao, Y., Lin, Y., Wang, Y., Yang, Z., Liu, J., Zhou, J., Yan, Y., and Huang, J. (2009). Metal-driven hierarchical self-assembled one-dimensional nanohelices. *Nano Lett.* 9, 4500–4504.
- Myllymäki, T.T.T., Nonappa, Yang, H., Liljeström, V., Kostianen, M.A., Malho, J.M., Zhu, X.X., and Ikkala, O. (2016). Hydrogen bonding asymmetric star-shape derivative of bile acid leads to supramolecular fibrillar aggregates that wrap into micrometer spheres. *Soft Matter* 12, 7159–7165.
- Travaglini, L., Bridgland, L.N., and Davis, A.P. (2014). Cholanamide components for organic alloys; expanding the scope of nanoporous steroidal ureas. *Chem. Commun. (Camb.)* 50, 4803–4805.
- Natarajan, R., Bridgland, L., Sirikulkajorn, A., Lee, J.-H., Haddow, M.F., Magro, G., Ali, B., Narayanan, S., Strickland, P., Charmant, J.P.H., et al. (2013). Tunable porous organic crystals: structural scope and adsorption properties of

- nanoporous steroidal ureas. *J. Am. Chem. Soc.* **135**, 16912–16925.
38. Kalenius, E., Groessl, M., and Rissanen, K. (2019). Ion mobility–mass spectrometry of supramolecular complexes and assemblies. *Nat. Rev. Chem.* **3**, 4–14.
 39. Lombardo, D., Kiselev, M.A., Magazù, S., and Calandra, P. (2015). Amphiphiles Self-Assembly: Basic Concepts and Future Perspectives of Supramolecular Approaches. *Adv. Condens. Matter Phys.* **2015**, e151683.
 40. Zhang, M., Strandman, S., Waldron, K.C., and Zhu, X.X. (2016). Supramolecular hydrogelation with bile acid derivatives: structures, properties and applications. *J. Mater. Chem. B Mater. Biol. Med.* **4**, 7506–7520.
 41. Mai, Y., and Eisenberg, A. (2012). Self-assembly of block copolymers. *Chem. Soc. Rev.* **41**, 5969–5985.
 42. Zhang, M., Fives, C., Waldron, K.C., and Zhu, X.X. (2017). Self-Assembly of a Bile Acid Dimer in Aqueous Solutions: From Nanofibers to Nematic Hydrogels. *Langmuir* **33**, 1084–1089.
 43. Travaglini, L., D'Annibale, A., di Gregorio, M.C., Schillén, K., Olsson, U., Sennato, S., Pavel, N.V., and Galantini, L. (2013). Between peptides and bile acids: self-assembly of phenylalanine substituted cholic acids. *J. Phys. Chem. B* **117**, 9248–9257.
 44. Giguère, G., and Zhu, X.X. (2010). Functional star polymers with a cholic acid core and their thermosensitive properties. *Biomacromolecules* **11**, 201–206.
 45. Likos, C.N., Sciortino, F., Zaccarelli, E., and Zihnerl, P. (2016). *Soft Matter Self-Assembly* (IOS Press).
 46. Stow, S.M., Causon, T.J., Zheng, X., Kurulugama, R.T., Mairinger, T., May, J.C., Rennie, E.E., Baker, E.S., Smith, R.D., McLean, J.A., et al. (2017). An Interlaboratory Evaluation of Drift Tube Ion Mobility-Mass Spectrometry Collision Cross Section Measurements. *Anal. Chem.* **89**, 9048–9055.
 47. Gabelica, V., Shvartsburg, A.A., Afonso, C., Barran, P., Benesch, J.L.P., Bleiholder, C., Bowers, M.T., Bilbao, A., Bush, M.F., Campbell, J.L., et al. (2019). Recommendations for reporting ion mobility Mass Spectrometry measurements. *Mass Spectrom. Rev.* **38**, 291–320.
 48. Frisch, M.J., Trucks, G.W., Schlegel, H.B., Scuseria, G.E., Robb, M.A., Cheeseman, J.R., Scalmani, G., Barone, V., Mennucci, B., Petersson, G.A., et al. (2013). Gaussian 09, Revision D.01. <http://www.rsc.org/suppdata/c5/sc/c5sc02423d/c5sc02423d1.pdf>.
 49. Linnanto, J., and Korppi-Tommola, J. (2004). Structural and Spectroscopic Properties of Mg–Bacteriochlorin and Methyl Bacteriochlorophyllides a, b, g, and h Studied by Semiempirical, ab Initio, and Density Functional Molecular Orbital Methods. *J. Phys. Chem. A* **108**, 5872–5882.
 50. Rigaku Oxford Diffraction (2017). *CrysAlis^{Pro}* Software system, version 38.46 (Rigaku Corporation).
 51. Sheldrick, G.M. (2015). Crystal structure refinement with SHELXL. *Acta Crystallogr. C Struct. Chem.* **71**, 3–8.
 52. Dolomanov, O.V., Bourhis, L.J., Gildea, R.J., Howard, J.A.K., and Puschmann, H. (2009). OLEX2: a Complete Structure Solution, Refinement and Analysis Program. *J. Appl. Cryst.* **42**, 339.